This paper can be found at https://doi.org/10.1016/j.autcon.2017.09.023

HERITAGE PRESERVATION BY COMBINING RADIOMETRIC AND GEOMETRIC ANALYSIS OF TLS DATA: THE SAN FRANCISCO MASTER GATE IN ALMEIDA (PORTUGAL)

Luis Javier Sánchez-Aparicio[1]*, Susana Del Pozo[1], Luís F. Ramos[2], Andrés Arce[2], Francisco M. Fernandes[3]

[1]*Department of Cartographic and Land Engineering. University of Salamanca, High Polytechnic School of Ávila, Hornos Caleros, 50, 05003, Ávila (Spain). L.J.S.A (luisj@usal.es), S.D.P (s.p.aguilera@usal.es)*

[2] *ISISE, Department of Civil Engineering, University of Minho, Campus de Azurém, 4800-058 Guimarães, Portugal. L.F.R. (*lramos@civil.uminho.pt*), A.A. (*aarce.cr@gmail.com*)*

[3] *ISISE, Faculty of Engineering and Technologies, University Lusíada - Norte, Famalicão, Portugal F.F. (*fmcpf@civil.uminho.pt*)*

**Corresponding author: Tlf.: +34 920353500; Fax: +34 920353501;*

E-mail address: luisj@usal.es

Abstract

Damage mapping is considered a critical stage in the correct diagnosis of the state of conservation of Cultural Heritage manifestations. The common approach generally implies a large user interaction to map the different pathological processes presented on 2D documents such as elevations or sections, among others. In contrast with this practice, the present paper proposes a semiautomatic 3D-methodology, with a minimum user interaction, able to accurately analyse both radiometric and geometric data recovered by a non-contact technology (Terrestrial Laser Scanning), allowing the extraction and quantification of a wide diversity of pathological processes from biological colonization to deformations. This approach is therefore a potential tool for the rapid and accurate diagnosis of Cultural Heritage. To confirm the applicability and potential offered by the proposed methodology, a highly affected historical masonry, the San Francisco Master Gate of the Almeida Fortress (Portugal), was evaluated by using the Faro Focus 3D 120 Laser Scanner.

Keywords: Historical constructions; Masonry construction; Damage mapping; Construction diagnosis; Terrestrial Laser Scanner; Radiometric classification; Geometric features.

1 Introduction

Currently, Cultural Heritage (CH) is considered not only a keystone in the economic development of a country but also a living witness of our age-old traditions [1]. For this reason, it is necessary to safeguard the authenticity and integrity of our Cultural Heritage for future generations [2].

Inside the wide variety of constructions that compose our CH assets, from religious buildings [3], to network infrastructures [4] or rock art manifestations [5], masonry is the most commonly used constructive solution. This popularity arises from its resistance to degradation agents compared with other materials such as wood or adobe [6,7]. However, the other constructive systems, biological colonization, salts, and moisture among others [8] can promote the deterioration of the ornamental pieces presented on the monument as well as a reduction of its service life [9].

Based on these considerations, several international documents such as the Venice or Krakow Charters [2,10] demand the use of rigorous multidisciplinary approaches to study the conservation state of our cultural legacy. The final aim is to preserve its authenticity and values and design suitable restoration strategies to preserve the monument through time according to some modern restoration principles [11].

The non-contact and accurate nature of Terrestrial Laser Scanners (TLSs) as well as the fast and dense data acquisitions place these sensors as one of the best solutions for the 3D digitalization [12] of CH assets. The 3D models obtained with these geomatic sensors are normally used to create complex CAD models for further structural evaluation [4,13,14] or used to extract elevations or section maps [15]. However, the potential of these sensors goes beyond a massive register of spatial coordinates, since they also store very useful radiometric information, the backscattered intensity data [16]. Using the combination of these two capabilities (radiometric and geometric), a laser scanner can be positioned as one of the most versatile tools to remotely study the conservation state of historical construction. In this way, a damage assessment can be

performed in three dimensions with the advantage of being able to quantify the damages mapped on the monument in contrast with more traditional practices of manual damage mapping on orthoimages or sections [15,17].

Under this assumption, this paper proposes a methodology to analyse together the radiometric and geometric data captured by TLS systems. The final goal is to develop a method capable of mapping a wide range of the most common damages of historical masonry construction promoted by the presence of chemical, biological and physical alteration agents. To validate the proposed strategy, a historical construction inside the Fortress of Almeida, in Portugal, was chosen as a case study: the San Francisco Master Gate.

Within this context, the paper has been organized as follows: Section 2 defines the sensor used to diagnose the state of conservation as well as the processing methodology that was followed; Section 3 describes the Almeida Fortress and the San Francisco Master Gate; Section 4 shows the results after applying the proposed methodology, and finally, Section 5 summarizes the conclusions arising from the use of TLS data to analyse pathologies of historical constructions as well as some future work.

2 Methodology for exploiting radiometric and geometric data from TLS point clouds

2.1 Terrestrial Laser Scanner

Due to the difficulty in accessing some parts of the case study as well as the unfavourable lighting conditions (shaded and lighted areas) to perform the data acquisition in some parts, the use of a TLS is the best solution given its active nature (independent of solar lighting conditions) and versatility. Specifically, the Faro Focus 3D 120 (FF3D120) (Figure 1) was the sensor used to evaluate the methodology proposed in this paper. The most relevant features of this TLS are specified in Table 1.

Table 1: FF3D120 technical specifications.

Physical principle	Phase shift
Wavelength (nm)	905 - near infrared
Measurement range (m)	0.6 - 120
Field of view (degrees)	360 H x 320 V
Accuracy nominal value at 25 m (mm)	2
Beam divergence (mrad)	0.19
Capture rate (points/sec)	122,000 / 976,000
Spatial resolution at 10 m (mm)	6
Radiometric resolution (bits)	11

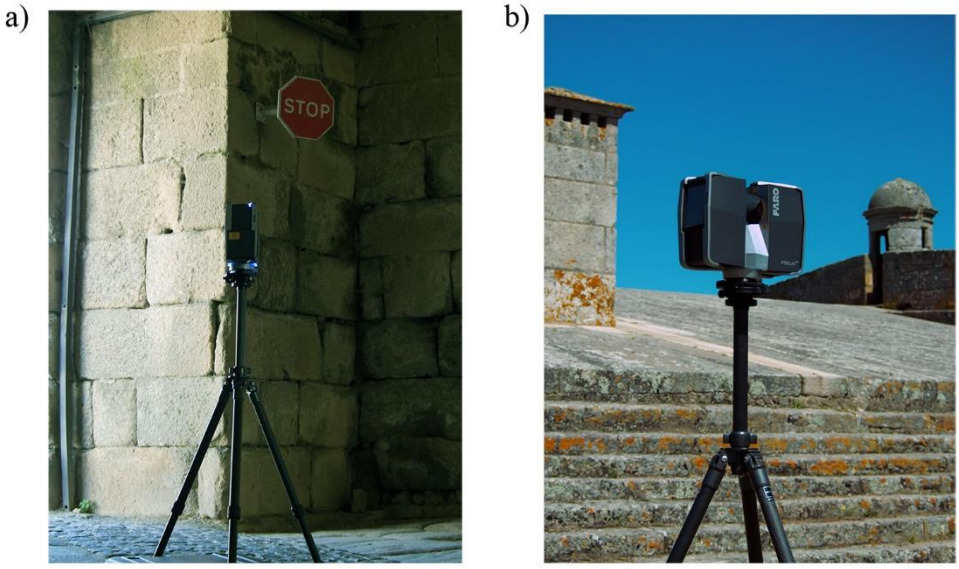

Figure 1: TLS system during the data acquisition: (a) inside the barrel vault and (b) on the roof

2.2 Processing of laser scanner data for damage detection

3 To make full use of the TLS data acquisition for damage detection, we have decided to exploit the dual applicability of this sensor, radiometry and geometry laser data. For that reason, the laser point cloud takes two different paths in the processing step, the red- and blue-shaded areas of Figure 2. This figure summarizes the processing workflow followed to finally obtain a complete diagnosis of the state of degradation of construction.

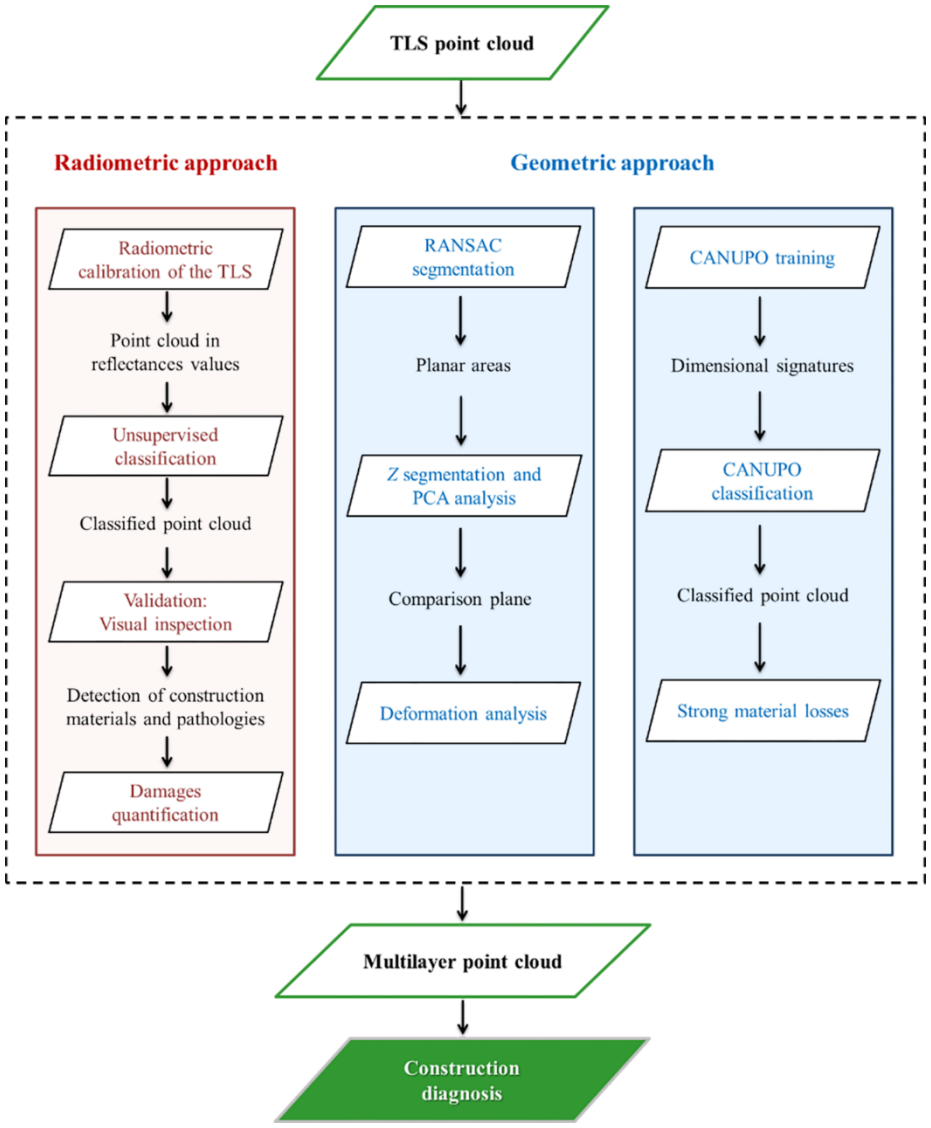

Figure 2: Scheme of the workflow followed to perform the mapping and evaluation of pathologies in the constructions.

The radiometric approach encompasses four processes: the radiometric calibration of the laser scanner, an automatic classification of the point cloud to map different pathologies, the validation of the classification by a visual inspection and the final quantification of damages. For its part, the geometric approach encompasses two parallel processes: on one hand, a planar extraction by means of the RANSAC shape detector, a *z* segmentation of the planes extracted to create the comparison plane and the analysis of the discrepancies between the planar clusters extracted and the comparison planes; and on the other hand, the CANUPO algorithm was trained and applied on the point cloud to evaluate those areas with strong material losses. Finally, with the results of

both approaches, a multilayer point cloud was created to make a comprehensive and rigorous diagnosis of the chosen construction considering both radiometric and geometric criteria.

3.1 Pre-processing

Historical constructions are geometrically characterized by their complexity and size, making necessary the use of several scanning positions to record the whole construction. Considering the complexity and size of the construction, the present methodology applied a coarse to fine strategy to register the different scans taken [14]. First, a pairwise alignment, by means of the Iterative Closest Point (ICP) algorithm [18], was used. Later, and with the aim of minimizing the error accumulation, a global registration based on the Generalized Procrustes Analysis (GPA) approach [19] was carried out. In this way, a dense and accurate 3D representation of the monument was obtained.

With the 3D representation of the monument, the next step required to diagnose the construction involves the extraction of the damage by the radiometric and geometric approaches proposed. In accordance with the visual indicators proposed by ICOMOS [8], the following pathological processes were evaluated: (i) deformations, (ii) disaggregation, (iii) biological activity, (iv) salt crust and (v) moisture.

3.2 Radiometric approach

Backscattered laser intensity generates very useful radiometric information to evaluate the object not only quantitatively but also qualitatively [16,20]. In this way, by using a single sensor, it is possible to perform very comprehensive and rigorous studies of the construction from which to derive both deformation and structural analysis as well as characterize visual indicators of degradation such as biological colonization or crusts.

In addition, if the laser intensity data are radiometrically calibrated, the range of studies will be broadened, allowing quantity and quality multitemporal analysis of the construction. In this procedure, the raw intensity laser signal (in digital values) is transformed into surface reflectivity

values. These values are inherent characteristics of each material (related to their physical properties), and thus, it is possible to define each one unequivocally. Thus, any alteration of a material will result in a change in the way the material reflects incident radiation and will therefore be captured by the sensor.

During the radiometric calibration, the following factors are considered globally relevant in the backscattered laser signal behaviour [21]: (i) the scanning geometry, (ii) the surface properties of the materials, and (iii) some instrumental parameters.

Two factors define the scanning geometry: (i) the distance between the scanner and the object, and (ii) the incoming beam incidence angle to the object [22,23]. The distance effect plays a strong role in TLS and consists of an attenuation proportional to the square of the distance considered usual. However, the two factors must be studied individually for each specific scanner since the instrumental effects depend on each specific device [24-26]. However, the incidence angle effect is related not only to the scanning geometry but also to the scattering properties of the object surface [27].

3.2.1 *Radiometric calibration of the TLS*

The FF3D120 was calibrated in a previous field campaign [9] for the range of distances between 9 and 36 m. This range has been extended from 3 to 36 m to use the calibrated laser intensity in field campaigns where a greater proximity to the object of study is required, as in the case study covered by this paper. Specifically, a reflectance-based radiometric calibration [28] consisting of analysing the distance-behaviour of the backscattered TLS radiation was performed by using the same equipment and methodology as was used in the previous experiment. Under laboratory conditions and in a completely dark room, a 4-panel Spectralon® was stationed at 0.5 m intervals from 3 to 9 m to be scanned (Fig. 3) at a resolution of 6 mm at 10 m to complete the range of distances of the previous calibration [16].

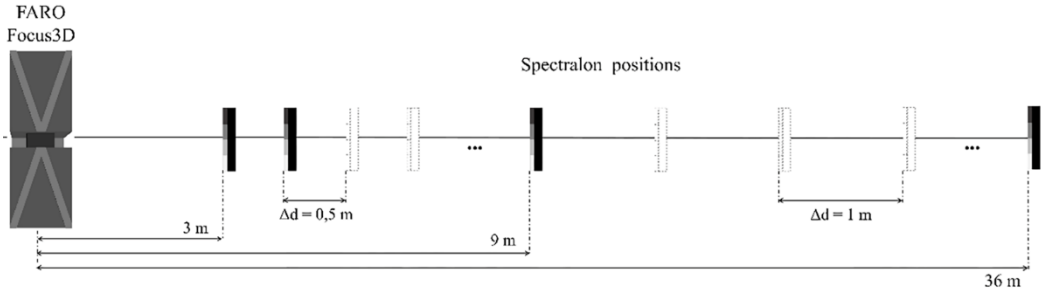

Figure 3: Illustration of the FF3D120 data acquisition design to study the behaviour of the backscattered intensity regarding different scanning distances.

Raw intensity data belonging to each reflectance panel (99%, 50%, 25% and 12% reflectance) were calculated by averaging the intensity values associated with the group of points belonging to each panel. Finally, the internal behaviour of the FF3D120 was modelled by comparing the mean intensity value per panel with the distance at which each acquisition was made, resulting in the graph illustrated in Figure 4.

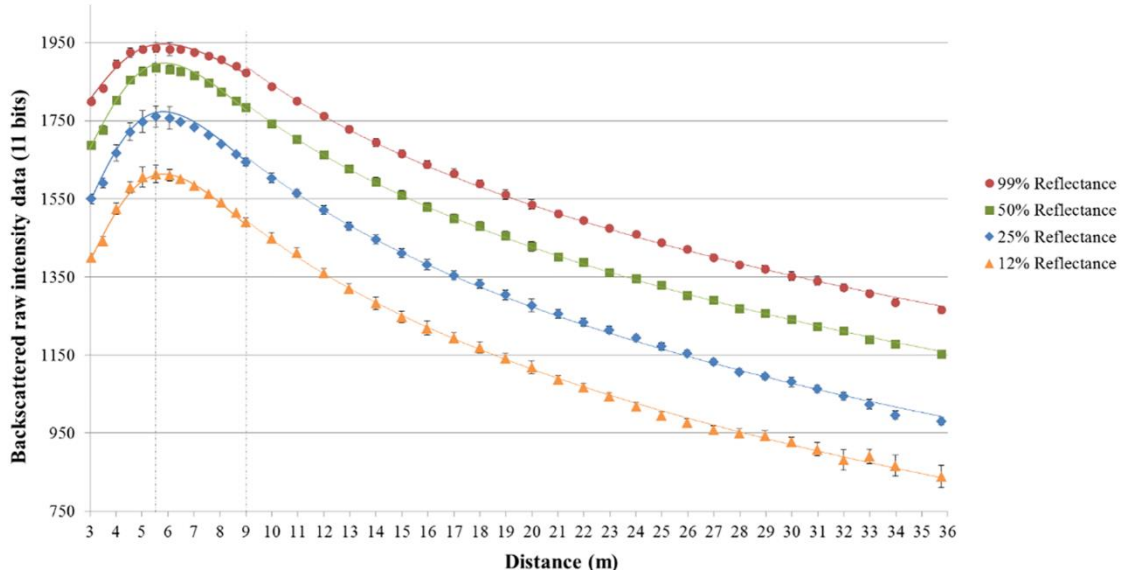

Figure 4. FF3D120 backscattered intensity behaviour with distance. Measurements from a 4-panel Spectralon placed at different distances increments.

For this range of distances, the logarithmic behaviour of the FF3D120 backscattered intensity data was adjusted using the next empirical equation (Eq. 1).

$$\rho_{range} = e^{a \cdot d} \cdot bd^2 \cdot e^{c1 \cdot I_F} \quad (1)$$

Table 2. Empirical coefficients obtained during the calibration campaign carried out.

Range of distances	a	b	c_1	R^2
3-5.25	-1.0928	3.029510^{-5}	0.006397	0.9868
5.25-9	-0.1134	4.944610^{-7}	0.005911	0.9932
9-36	0.0214	3.907210^{-7}	0.005415	0.9966

Table 2 shows the coefficients obtained for the calibration of the FF3D120, where *a* and *b* are two empirical coefficients related to the signal attenuation and internal conversion from the received power to the final digital levels, *d* is the distance between the laser scanner and the measured object, *c1* is the gain of the TLS and I_F is the raw intensity data in digital levels (11 bits).

Once the calibration is done, the intensities of points corresponding to the proportion of radiation reflected by each surface are expressed in reflectance (% of reflected radiation) instead of digital levels.

3.2.2 *Incidence angle affectation*

The incidence angle (α) of the laser beam is an important factor that affects the received intensity according to Lambert´s Law [29]. The incidence angle is defined as the angle between the surface normal, obtained through the Principal Component Analysis of the surface (PCA), and the incoming laser shot ray. For ideal Lambertian scatters, the reflected intensity is proportional to $\cos \alpha$. The higher the incidence angle of the laser beam, the smaller the amount of light coming

back to the sensor. In this study, due to the lack of information about the reflection characteristics (BRDF index) of each of the materials to be measured, it has been assumed that all the surfaces have a Lambertian behaviour.

By applying the following equations (Eq. 2 and 3), it is possible to correct the backscattered laser radiation from the incidence angle affectation considering for this purpose the surface normal, calculated during the pre-processing phase (Section 2.2.1).

$$\rho_{905nm} = \frac{\rho_{range}}{\cos \alpha} \tag{2}$$

$$\alpha = acos \frac{\vec{u} \cdot \vec{v}}{|\vec{u}| \cdot |\vec{v}|} \tag{3}$$

where $\vec{u}$ is the normal vector to each point of the point cloud, $\vec{v}$ the beam-directing vector and $|\vec{u}|$ and $|\vec{v}|$ the magnitude of each vector.

3.2.3 *Classification procedure*

For the pathological evaluation through the radiometric approach, an automatic clustering categorization has been performed to group 3D point clouds in different "clusters" [30] by analysing, in this case, the calibrated intensity data (reflectance) through an unsupervised classification method. Thus, points that are grouped together have reflectance like each other.

A variety of algorithms perform this kind of classification. The Fuzzy K-means clustering algorithm [31], one of the most widely used and the one being used in this work, consists of minimizing the squared distance between feature values of two points that reside in the same cluster. The approach on which the centre of each cluster is solved finds the minimum of a sum-of-squares cost function (Eq. 4) using coordinate descent.

$$J_q(U,V) = \sum_{j=1}^{N}\sum_{i=1}^{K}(u_{ij})^q\, d^2\left(X_j, V_i\right); \quad K \le N \tag{4}$$

where q is any real number greater than 1 and is the weighting exponent for u_{ij} that controls the "fuzziness" of the resulting clusters, U is a $N \times K$ partition matrix where N is the number of data points and K the number of clusters, $V=\{V_1, V_2,\ldots, V_K\}$ is a set of objects in the same object domain, X_j is the j^{th} m-dimensional feature vector, V_i is the centroid of the i^{th} cluster, u_{ij} is the degree of membership of X_j in the i^{th} cluster and $d^2\left(X_j, V_i\right)$ is any inner product metric (distance between X_j and V_i).

Fuzzy partitioning is carried out through an iterative optimization of the cost function shown above (Eq. 4), with the update of membership u_{ij} and the cluster centres $\widehat{V_i}$ by Eq. 5

$$u_{ij} = \frac{\left[\frac{1}{d^2(X_j, V_i)}\right]^{1/(q-1)}}{\sum_{k=1}^{K}\left[\frac{1}{d^2(X_j, V_k)}\right]^{1/(q-1)}}, \qquad \widehat{V_i} = \frac{\sum_{j=1}^{N}(u_{ij})^q\, X_j}{\sum_{j=1}^{N}(u_{ij})^q} \tag{5}$$

This iteration will stop when $\max\left[\left|u_{ij} - \hat{u}_{ij}\right|\right] < \varepsilon$, with ε as a termination criterion between 0 and 1. This method converges to a local minimum or a saddle point of J_q.

3.3 Geometric approach

Complementary to the radiometric data acquired by TLS systems, geometrical features stored in the point cloud, such as normals or the dimensionality of the points, can be used to detect additional pathological processes such as deformations or material losses.

The deformation evaluation can be carried out following two approaches [17,32]: (i) direct point to point comparison and (ii) point to primitive distance evaluation. Regarding the first approach, at least two point clouds are required to compare different states. Meanwhile, the second approach requires a point cloud segmentation into different components. Components that later are fitted to primitives and compared with the original point cloud. Considering the lack of previous data,

the second approach was used to estimate the deformation of different elements of the construction.

Inside the wide variety of constructive elements present in a historical building, planes (façades or roofs) are one of the most common primitives. Therefore, a suitable strategy was necessary to extract all the points in the point cloud and affect them to a particular primitive. For this purpose, the RANSAC Shape Detection algorithm [33] was used.

However, primitives extracted by means of the RANSAC algorithm cannot be considered representative, being influenced by the current deformation state (considering that the plane extracted was initially a perfectly plane). To minimize this influence, a *z* segmentation was carried out to extract all those points between two z values (e.g., points that belong to the first two rows of masonry blocks) followed by a Principal Component Analysis (PCA) to extract the maximum dispersion and the centroid of these points (façade direction). Finally, a reference plane was created with the maximum dispersion vector, the centroid, as well as a second point obtained by sifting the *z* value of the centroid (Fig. 5).

For the case of non-vertical planes (e.g., roof planes) and during the *z* segmentation stage, an additional PCA analysis was carried out to align the minimum (normal vector) and maximum dispersion directions with the *x* and *y*-axis, respectively.

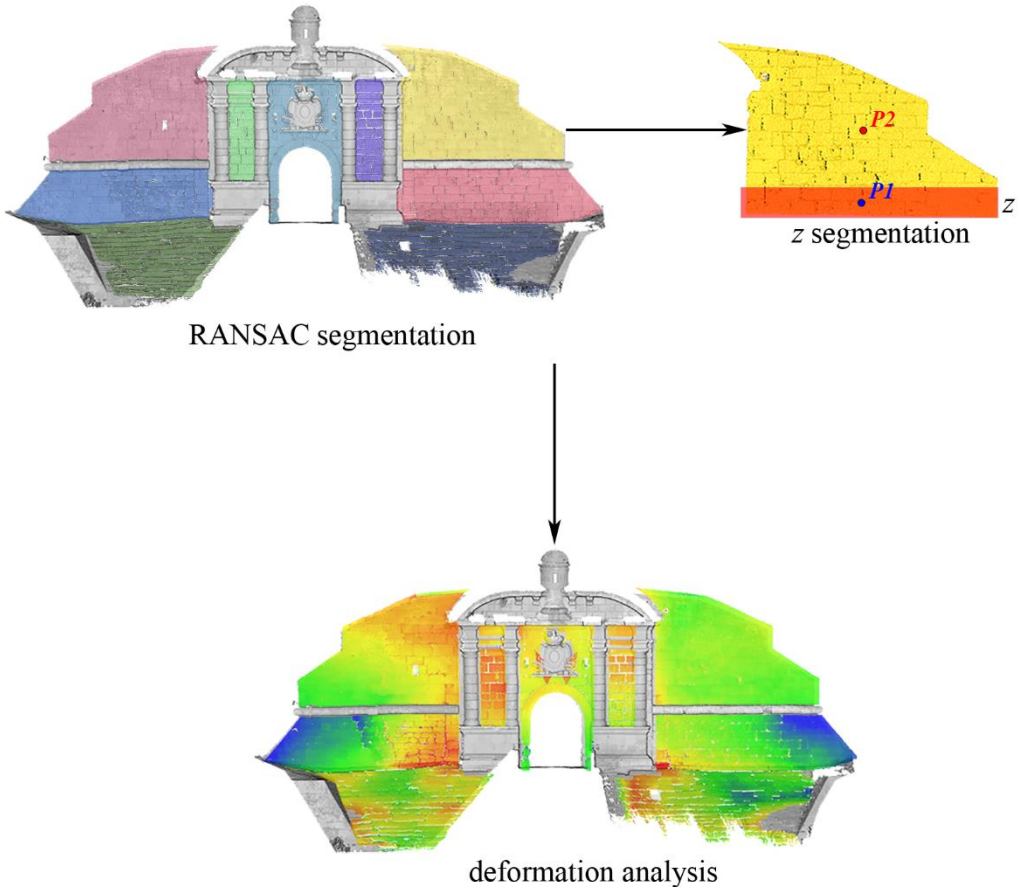

Figure 5: Graphical representation of the workflow followed to evaluate the deformations in the façade.

However, material disaggregation is a common pathological process in masonry constructions for which the procedures defined previously cannot provide a suitable solution.

Generally, at the block scale, simple masonry constructive elements such as barrel vaults can be interpreted as planar surfaces. Meanwhile, the loss of material can be interpreted as a local 3D feature. Thus, the analysis of the dimensionality of the point stands as a possible solution to characterize the pathological process. Considering this analysis, the CANUPO algorithm [34] was applied to detect those areas with a strong lack of material, comprising the following stages: (i) a first training phase, and (ii) a final classification stage.

During the training phase, several local dimensionality analyses were carried out to characterize the point cloud at different scales (1D dimensionality indicates that points at this scale belong to a line, 2D to a planar surface and 3D to a volumetric surface). Finally, a Linear Discriminant Analysis is applied to find the hyperplane of the maximal class separability [34] (Fig. 6).

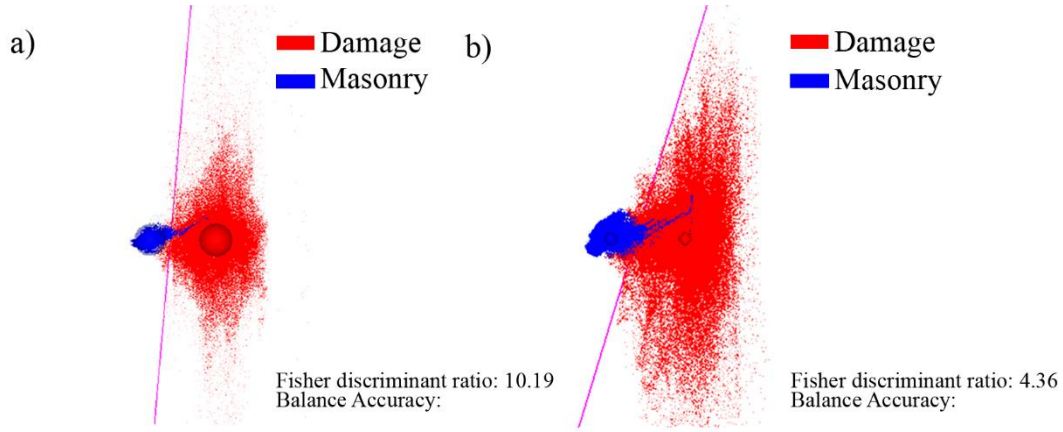

Figure 6: Results during the CANUPO training: (a) Classifier A; (b) Classifier D. In red is the damage class, in blue masonry and in magenta the hyperplane of maximal separability.

Once the classifier is trained, points can be clustered into one of the two predefined classes during the training stage, allowing the segmentation of the point cloud. For the present case study, the predefined classes were masonry and damages.

4 Case study: Almeida Fortress

The Fortress of Almeida is a bulwarked fortification that, although it has been classified as "National Monument" since February 1928, wishes to break barriers, clearing the path that leads to a global projection as a UNESCO World Heritage site [35].

The desire for conservation of the heritage in Almeida is evident because not only has part of the ruined heritage been recovered, but also, the priority has been given to give new life to these spaces, transforming them into museums, offices and diverse spaces for the benefit of the community. This determination was based on several initiatives: seminars, research work, protocols with universities and technical schools that have given shape, step by step, to a sense of sustainable safeguarding [35].

4.1 Historical background

The Fortress of Almeida, composed of six bastions that form a star, is in the heart of the historical city of Almeida near the city of Guarda, Portugal (Fig. 7a). This military infrastructure was erected on the east side of the Côa River, and due to its strategic location, the city was condemned to be a place of war (Fig. 7b).

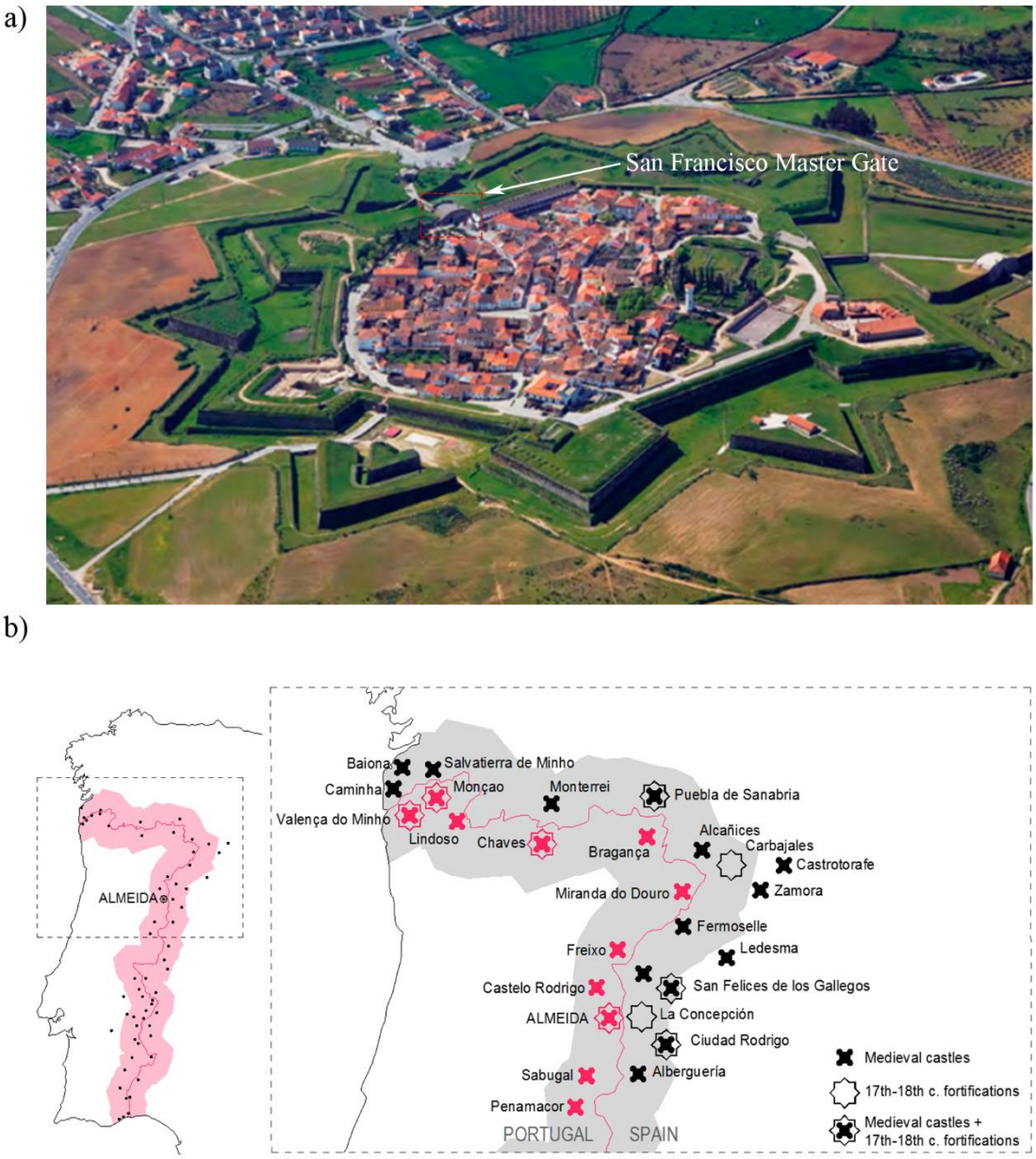

Figure 7: Location of the Almeida fortress: (a) Aerial view of the Almeida fortress [4] and (b) Spatial disposition of the military fortifications along the border between Spain and Portugal, based on [36] and [37].

In the Middle Ages and until 1297, Almeida was a space for dispute between Christians and Muslims. Later, the city was a victim of constant sieges and attacks due to the conflictive climate that appeared after the independence from the Castilian Kingdom of Leon during the 13th century [35]. During these tormented periods, the fortress was the focus of several constructions, demolitions and reconstructions. For more details, see [36].

4.2 The Master Gate of San Francisco

Placed as one of the Master Gates of the Almeida fortress, the construction of the Gate of San Francisco began between 1661 and 1667. The geometry of the wall was envisioned in such a way that the inclination angle made projectiles bounce in the direction of the enemies, and the massive amount of earth acted as a cushion partially absorbing the impact of projectiles [35]. Regarding the structural composition, two parts can be highlighted (Fig. 8): (i) a curved barrel vault that acts as a tunnel, allowing the transit into the city, and (ii) a lateral camera, which used to be the house of the guard. This second section is believed to have been added between 1744 and 1789. Also during this period, restoration works were carried out to replace damaged stones with new ones.

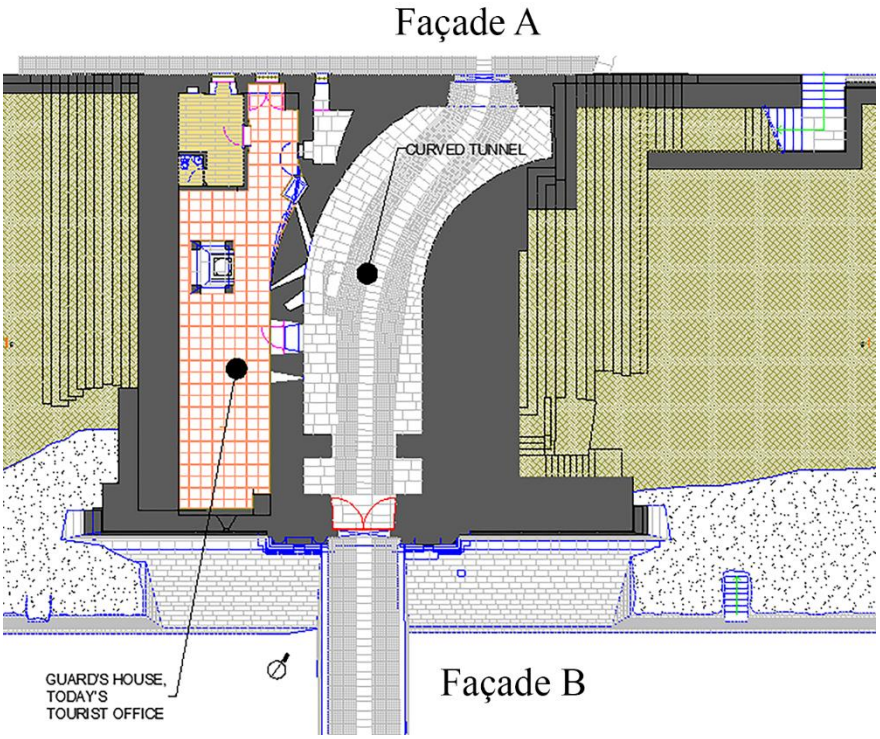

Figure 8: Plant view of the San Francisco Master Gate.

316 The French invasion in 1810 will pass down in history as the most destructive event both for the
317 fortress and the Master Gate of San Francisco. The constant bombing and the explosion of the
318 gunpowder storehouse destroyed the castle and generated great damage to the fortress and
319 specifically to this Master Gate. By 1815, the order to start reconstruction work on the Gate was
320 issued, although since the war ended in 1814, the urgency of reconstruction was low and the
321 construction works were kept to a minimum. It was not until the 1960s that a significant
322 restoration project occurred (Fig. 9).

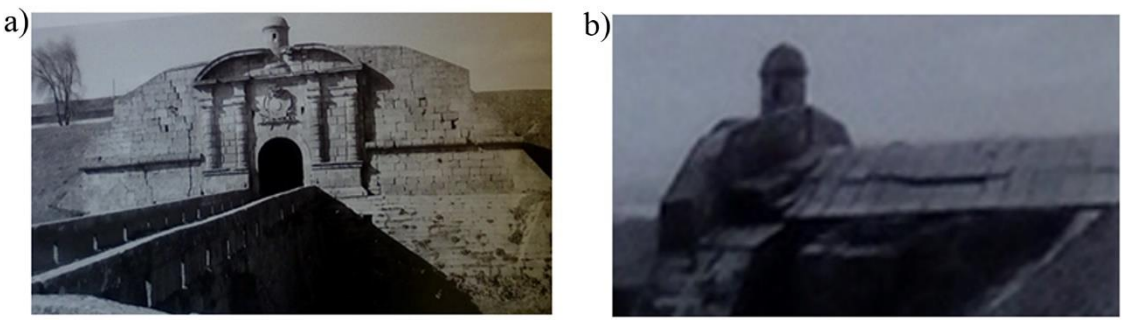

323

324 **Figure 9:** State of damage in the Master Gate of San Francisco in 1962: (a) façade B with vertical cracks and loss of
325 material; and (b) crack on the roofing system (stone roof).

326

327 In 1986, work continued in the San Francisco Master Gate, where the right side urgently needed
328 consolidation and cleaning of the masonry. The mortar used during this restoration was a
329 hydrophobic mix with cement with an estimated proportion of 1:2/3:6 (cement:lime:sand) [35].
330 Figure 10 shows its current aspect.

331

332

333

334 **Figure 10:** Current aspect and state of conservation of the San Francisco Master Gate [4].

335

336 **5 Damage mapping results**

337 **5.1 Data acquisition: San Francisco Gate scenario**

338 To build the 3D model of the Gate, twenty-six scans were needed to capture the whole structure:
339 (i) eleven scans to represent the façades, (ii) five stations to capture the barrel vault, and (iii) ten
340 scans to represent the roof of the construction. The huge amount of data captured, with a total of
341 712,324,286 points, required an optimization of the point cloud for further evaluations. Therefore,
342 two filters were applied previously to the registration stage: (i) distance filter with an average
343 threshold of 15 m, and (ii) a density filter to delete all the points that have neighbours closer than
344 5 mm. Then, the coarse to fine registration strategy defined in Section 2.4 was carried out. As a
345 result, a complete and accurate 3D representation of the Gate was obtained, composed of
346 104,451,530 points (14% of the original point cloud), with a registration error of 0.005 ± 0.003
347 m (Fig. 11).

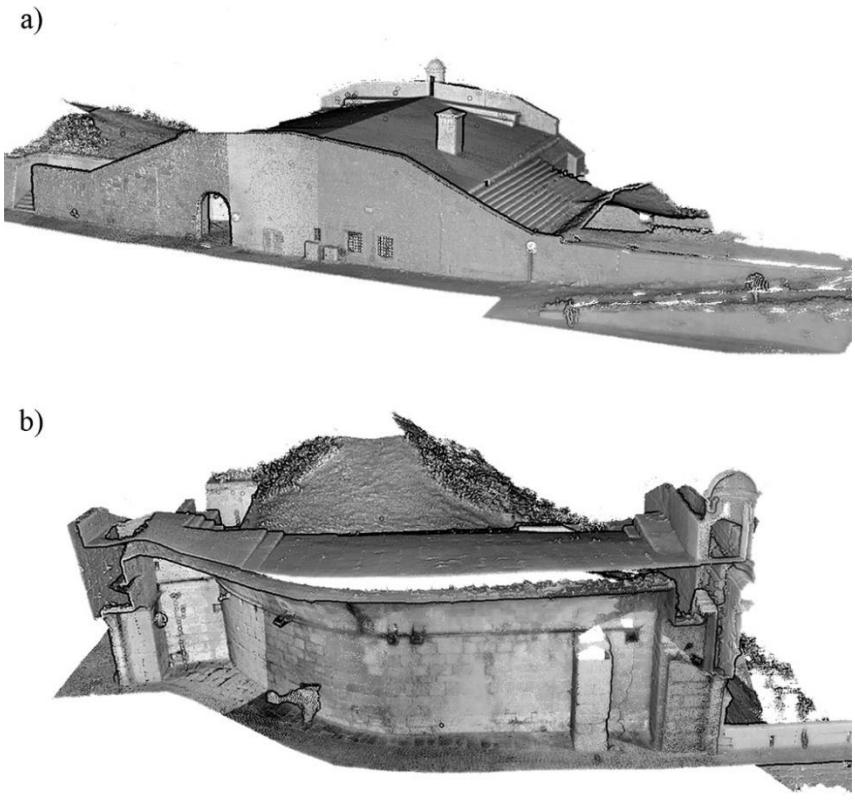

348

Figure 11: Registered point cloud: (a) Isometric view of the San Francisco Master Gate; (b) Longitudinal section across the barrel vault.

Considering the results provided by a visual inspection, the following constructive elements were evaluated: (i) façades A and B, (ii) roof, and (iii) barrel vault through the approaches defined in Section 2.

5.2 Results of the radiometric approach

5.2.1 *Point cloud models in reflectance values*

According to the methodology explained in Section 2 and illustrated in Figure 2, the characterization of visual indicators of damage in the selected constructive elements (façades and barrel vault) were evaluated. To that end, a radiometrically calibrated TLS was used to analyse the backscattered intensity in surface reflectivity values instead of raw digital levels (Fig. 12).

Calibrated point clouds show a great difference in terms of contrast. In the raw point cloud, radiometry is more homogeneous for the whole construction, and there are fewer differences between materials and possible pathologies than in the calibrated models.

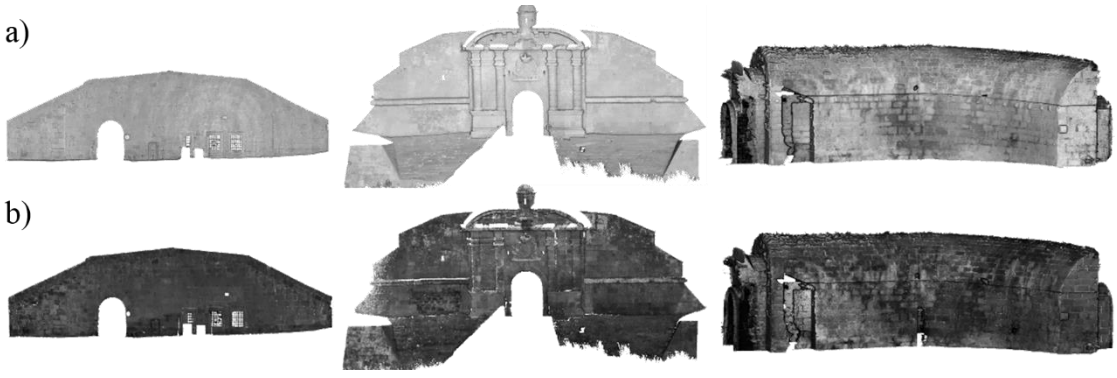

Figure 12: Comparison between the point clouds: (a) raw intensity data in digital levels and (b) in reflectance values after applying the radiometric calibration.

Having 3D models in reflectance values offers many other advantages than better visual appearance. On the one hand, they allow the evaluation of the evolution of pathologies through time, because by correcting the raw intensity data, laser acquisitions become invariant by the scanning geometry, that is, unaffected by the acquisition distance and the beam incidence angle [22]. Finally, by analysing physical values (inherent to each material) instead of digital levels provided by the internal electronics of the laser, studies become more rigorous, improving the accuracy of the classification [26,29]. This last advantage also allows us to evaluate, by comparing with available spectral libraries, whether the identification of materials and pathologies is more or less accurate.

5.2.2 *Classified point cloud*

To assess the potential of the proposed radiometric approach for detecting pathologies, three automatic classifications of the models were performed, establishing four, five and six clusters. Thus, the most suitable number of clusters for this dataset and for the wavelength of the laser scanner (905 nm) was evaluated. The mean reflectance and its standard deviation for each of the clusters were calculated according to the three unsupervised classifications performed. Finally, five clusters were chosen as the best option since the separability between the clusters of this classification was the optimum among the three performed (Table 3). In this case, a small overlap of 1.25% occurred between cluster 4 and cluster 5 but was assumed to be acceptable (Fig. 13) since it remains within the range of error estimated for this calibration technique (approximately 5%).

Table 3. Spectral behaviour of each cluster.

	Surface reflectivity (%)	
	Mean	Standard Deviation
Cluster 1	5.27 %	2.64 %
Cluster 2	14.91 %	6.31 %

Cluster 3	36.35 %	7.84 %
Cluster 4	57.25 %	8.86 %
Cluster 5	73.95 %	9.10 %

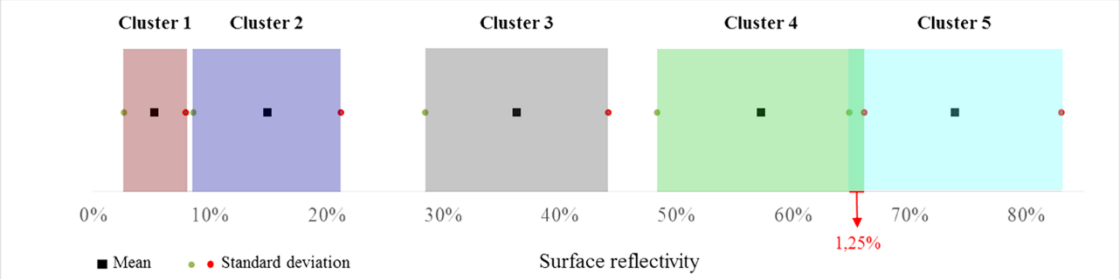

Figure 13: Graphical representation of the separability between clusters. It is worth mentioning the presence of a little overlap between cluster 4 and 5.

By applying the Fuzzy K-means clustering algorithm [31], each point of the point cloud was coloured according to the more related cluster of the five established for the three constructive elements studied. As Figure 14 shows, in all three classified models, there were areas with some pathologies. Taking a visual inspection of an expert into account, clusters were associated with the construction material and/or pathology with real meaning.

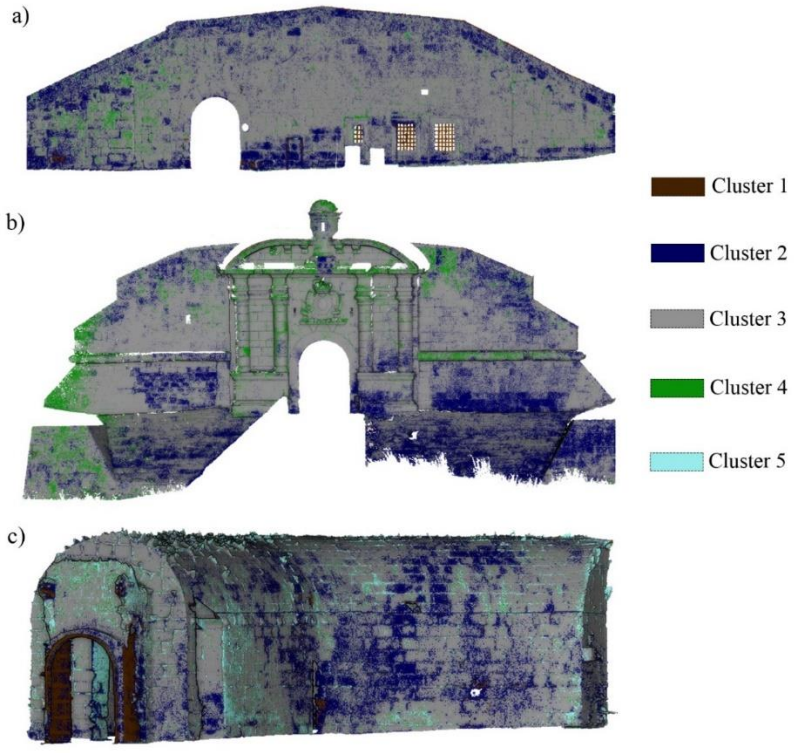

Figure 14: Results obtained for the Fuzzy-kmeans unsupervised classification carried out: (a) façade A; (b) façade B; and (c) barrel vault.

5.2.3 *Validation of the classification and damages quantification*

To validate this methodology, a comparison between the analysis results and real photographs (Fig. 15) was carried out. Comparing the five classified clusters with the informational classes provided by an expert visual inspection, it is possible to make the following correspondences: (i) Cluster 1 corresponds to wood or iron materials, (ii) Cluster 2 to humid areas and black deposits, (iii) Cluster 3 to granite stones, (iv) Cluster 4 to areas with presence of any type of biological colonization, and (v) Cluster 5 to salt crusts.

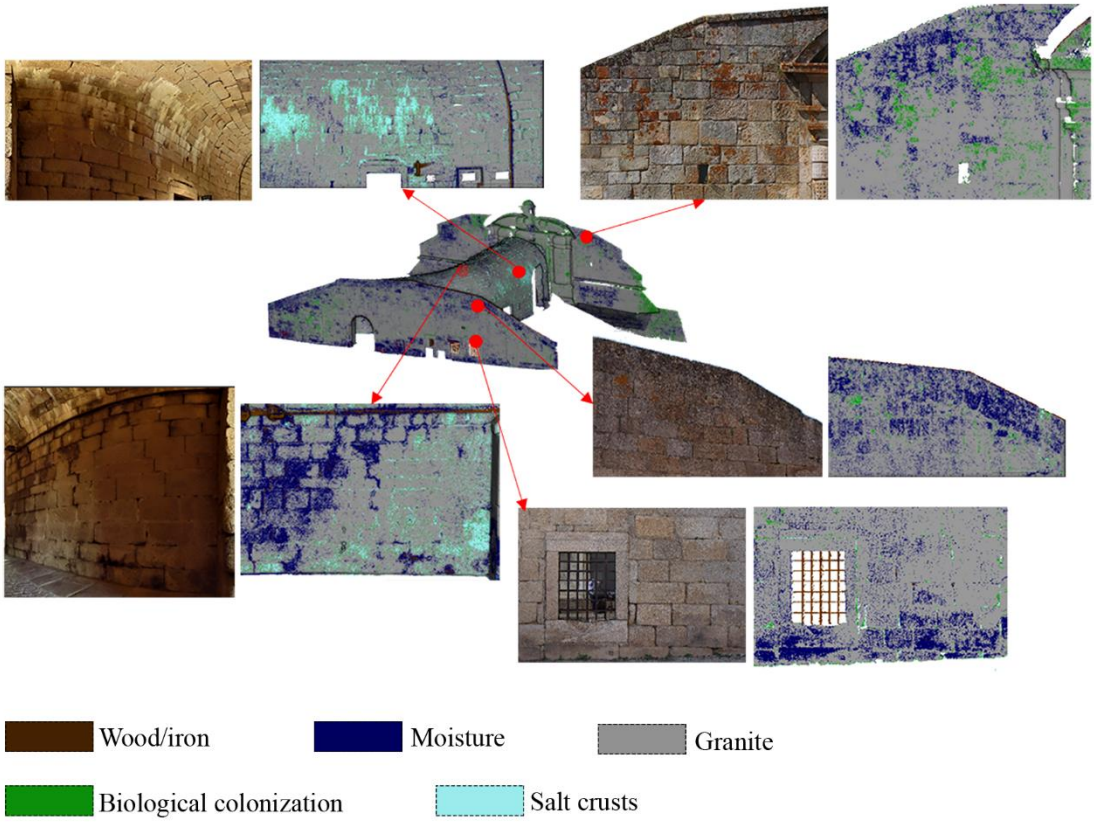

Figure 15: Validation and interpretation of the classification through an expert visual inspection.

Regarding wood and iron built-up surfaces, it was not possible to distinguish between them since they have a close surface reflectivity [40] of approximately 6% ± 3% at the wavelength for which the FF3D120 operates (905 nm). Thus, areas with these construction materials were classified together among the same cluster.

Table 4 quantifies the percentage of each of the materials and pathologies detected for the three analysed construction elements. The sum of points belonging to each cluster (expressed as a percentage) regarding the total number of classified points is shown in this table.

Table 4. Proportion of each information class extracted during the radiometric evaluation.

Classes:	Façade A	Façade B	Barrel vault
Wood/Iron	0.95 %	0.08 %	2.28 %
Granite (undamaged)	80.43 %	81.42 %	71.37 %
Moisture	15.82 %	12.52 %	15.83 %
Biological colonization	2.32 %	5.96 %	2.67 %
Salts	0.48 %	0.02 %	7.85 %

Focusing on the pathological analysis, the results show that in the three analysed locations, there is a high percentage of moisture (black deposit) (Fig. 15). In contrast, there is not a similar presence of biological colonization or salts in the three constructions. Façade B presents a greater affection for biological colonization (mainly orange lichens) due to its orientation, and the barrel vault has a larger area affected by efflorescence than the rest.

5.3 Evaluation of the geometric features: deformations and erosions

5.3.1 *Deformations*

The next process aims to evaluate the current deformation state of the selected constructive elements of the case study: (i) façade A, (ii) façade B, and (iii) roof, following the method proposed in Section 2.5 with a *z* value of 0.80 m (a height of two masonry blocks).

Regarding façade B, several planes were obtained by means of the RANSAC shape detection, requiring an additional clusterization process. This segmentation was based on the similarity, in terms of plane normal and centroid position, between clusters (Fig. 16, 17 and 18).

436
437 **Figure 16:** Segmentation carried out on façade B: (a) clusters obtained through the RANSCAC shape detector; (b)
438 planes clustered according with their similarity.

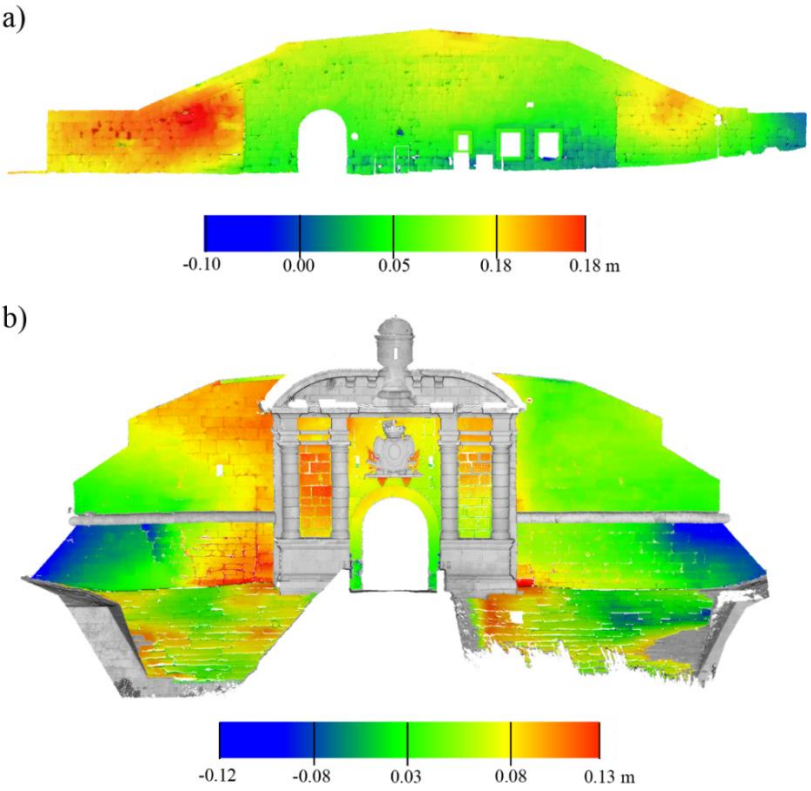

439
440 **Figure 17**: Results obtained during the deformation analysis: (a) façade A, with a unique vertical plane; and (b)
441 façade B with vertical and non-vertical planes.

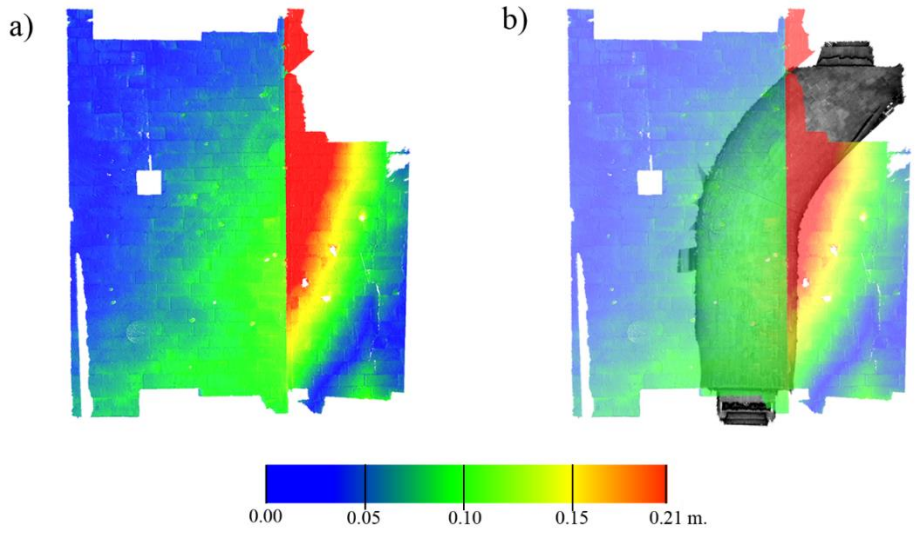

Figure 18: Deformation analysis carried out on the roof: (a) graphical representation of the results obtained; (b) relation between the roof´s deformation and the barrel vault position.

5.3.2 *Erosions*

Results obtained after the radiometric approach carried out on the barrel vault highlight a strong presence of salts and moisture (Fig. 19). These pathological processes, which promote the blistering of the masonry blocks (especially on the joints), are characterized by a local change in the dimensionality of the constructive element. Therefore, they require the use of an additional strategy to characterize these areas (Fig. 19).

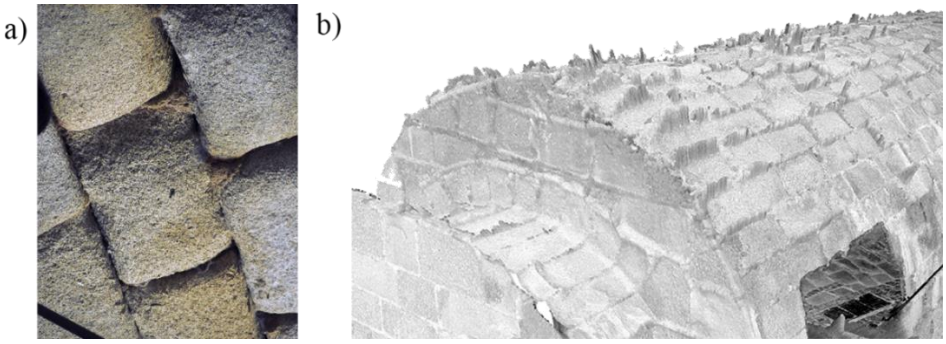

Figure 19: Block´s blistering (a) Photo taken during the visual inspection; (b) Detail of part of the barrel vault point cloud.

Considering this additional strategy, several CANUPO classifiers were trained, using for this purpose the average dimensions of the masonry block (0.90 × 0.40 m) as well as different

intervals (from 0.05 to 0.10 m) as possible work scales. Complementary, and with the aim of evaluating the performance of the algorithm, two quality analyses were used. On one hand, a quantitative evaluation was performed by means of the Balance Accuracy (*ba*) and the Fisher Discriminant Ratio (*fdr*) [20]. On the other hand, a qualitative analysis was performed through a visual evaluation of the results obtained (Table 5) (Fig. 20).

Classifier A shows the best qualitative and quantitative results (Table 4). However, it is possible to observe the presence of a high number of false negatives (Fig. 20a). This phenomenon arises from the block and the joint roughness on small scales, showing a dimensionality response similar to the eroded parts. According to this response, classifier A was tuned by manually changing the hyperplane position (classifier A_mod). This modification declined the quantitative indices (Table 5) slightly but, from the qualitative point of view, led to more accurate results (Fig. 20b).

Table 5: Performance of the CANUPO algorithm, at different configurations, in terms of Balance Accuracy and Fisher Discriminant Ratio.

Classification	Work scale			*ba*	*fdr*
	Maximum	Interval	Minimum		
A	0.90	0.05	0.05	0.99	10.19
B	0.90	0.10	0.05	0.99	7.80
C	0.40	0.05	0.05	0.97	6.91
D	0.40	0.10	0.05	0.96	4.36
A_mod	0.90	0.05	0.05	0.93	10.13

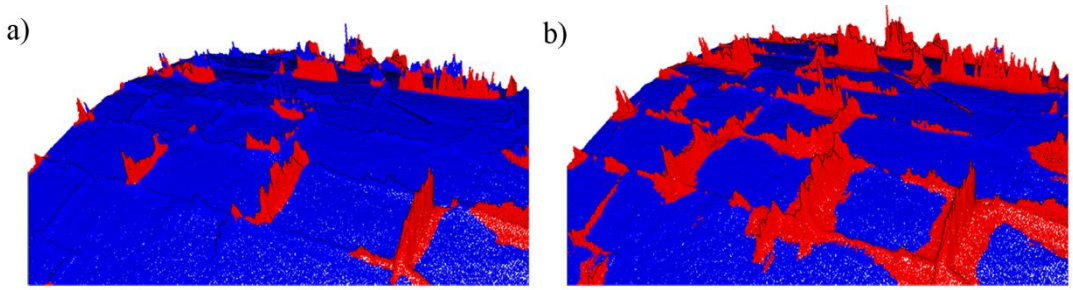

Figure 20: Results obtained during the training phase, in red are the damage areas and in blue non-damaged areas: (a) Classifer A; (b) Classifier A_mod.

Considering the A_mod classifier as the most appropriate classifier, the whole barrel vault was evaluated (Fig. 21).

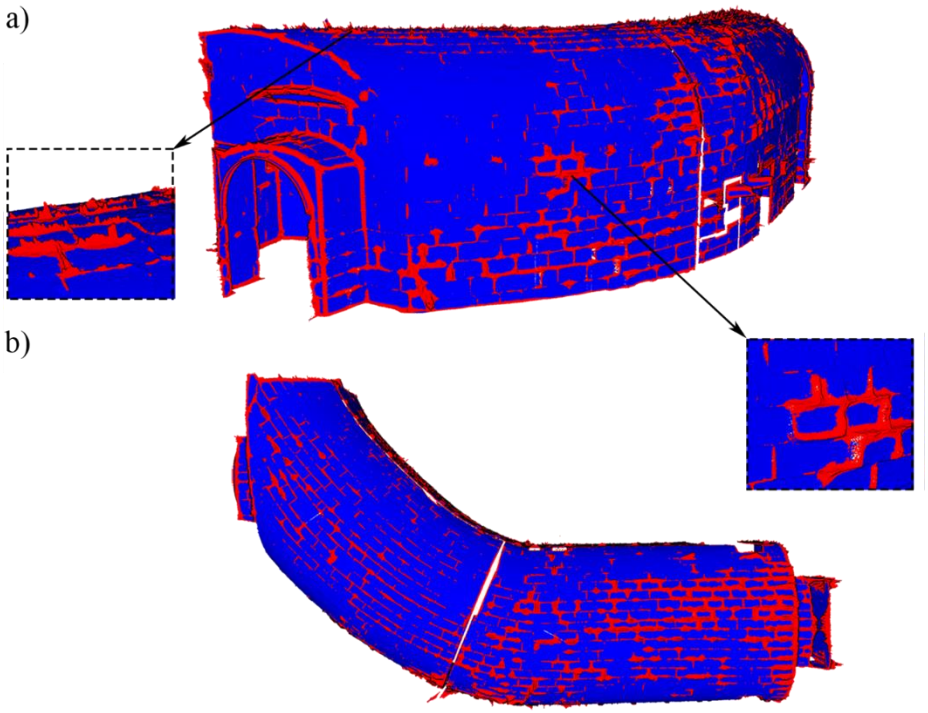

Figure 21: Point cloud segmented by the A_mod classifier (in red are the damage areas, in blue non-damage areas): (a) isometric and (b) plant view of the of the barrel vault.

In general terms, the CANUPO approach shows excellent correlation with the damage exhibited on the barrel vault (Fig. 21a), highlighting the most eroded parts of the structure. However, some mismatches can be found on the edges of the point cloud as well as in the shadow areas, suggesting the need to use additional filters to enhance the results obtained.

5.4 Comprehensive approach to damage analysis: the multilayer point cloud

At this point of the methodology, it has been possible to map a wide variety of pathological processes through the different approaches defined and carried out by the proposed methodology. Both radiometric and geometric methods add new layers of information to the original values of the point cloud (*x*, *y*, *z*, *intensity*) referenced in the same coordinate system, allowing the creation of a multilayer point cloud with information, not only about the geometric disposition of the construction but also about the damage presented on the construction (Fig. 22a).

Considering the pathologies detected at the barrel vault, an analysis of the most important parts (areas with strong erosion as well as the presence of moisture or salt crusts) was performed, combining the results provided by the radiometric classification with the results obtained by the CANUPO classifier (Fig. 22b).

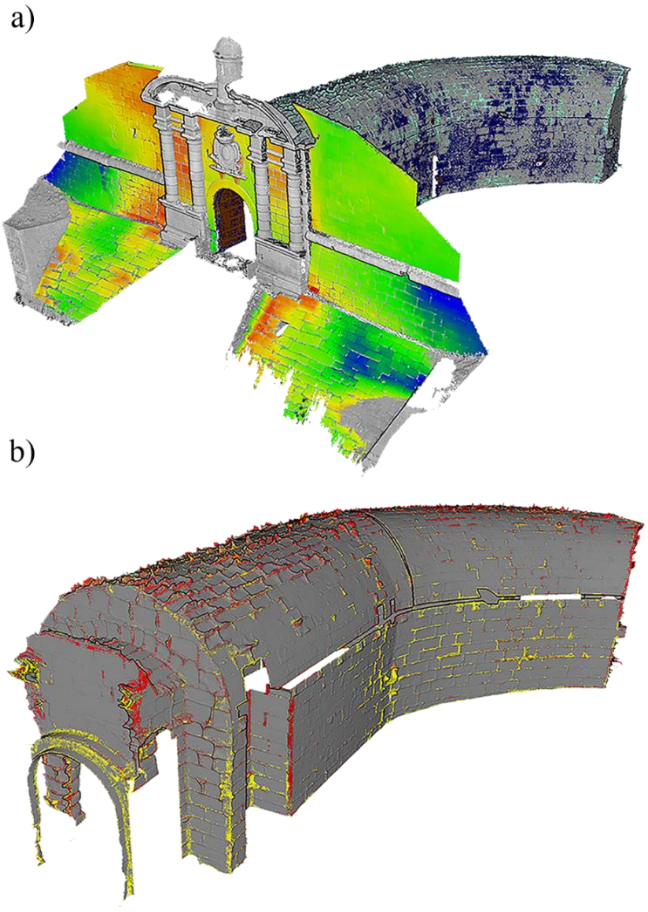

Figure 22: Multilayer point cloud: (a) isometric view with the deformation state of the façade B and the pathological processes detected by radiometry on the barrel vault; (b) relation between pathological processes presented on the barrel vault. In red, areas affected by strong erosions and salts, in yellow areas with erosions and moistures.

5.5 Diagnosis of the conservation state based on the multilayer point cloud results

The present experimental campaign carried out on the Master Gate of San Francisco corroborates the strong presence of pathological processes that are promoting the loss of material on ornamental pieces and masonry blocks.

On the façades, it is possible to observe the presence of biological activity, mainly nitrophilic lichens, and moisture (which generates black deposits on the masonry blocks) colonizing approximately 4.14% and 14.17%, respectively, of the total surface (Fig. 14). Regarding the biological colonization, façade B shows higher activity (5.96% in contrast with the 2.32% of façade A), especially on the cornice, probably due to its situation (in an open space) and orientation (south). However, façade A shows a large area affected by moisture (15.82%), in part promoted by its orientation.

With respect to the deformations, façade A shows out-of-plane deformations (with a maximum displacement of 0.18 m) on the lateral retaining walls (Fig. 17b). Those two walls are completely split for the gate building by a construction joint (Fig. 23). On the left side, the maximum deformations are close to 0.18 m but with a random distribution without showing the tilt of the wall. This deformation could be due to a construction defect. On the other side, the maximum deformation appears on the top of the wall, indicating a local tilt on the wall or a bubble in the wall. The maximum value is also close to 0.18 m (Fig. 17b). Concerning Façade B (Fig. 17a), it is possible to observe out-of-plane deformations on the vertical plane of the façade. No tilting configuration is visible, since the deviations are almost constant with a maximum of 0.13 m. The deviations are most probably due to construction defects or derived from the intensive reconstruction carried out during 1986 (Fig. 9a).

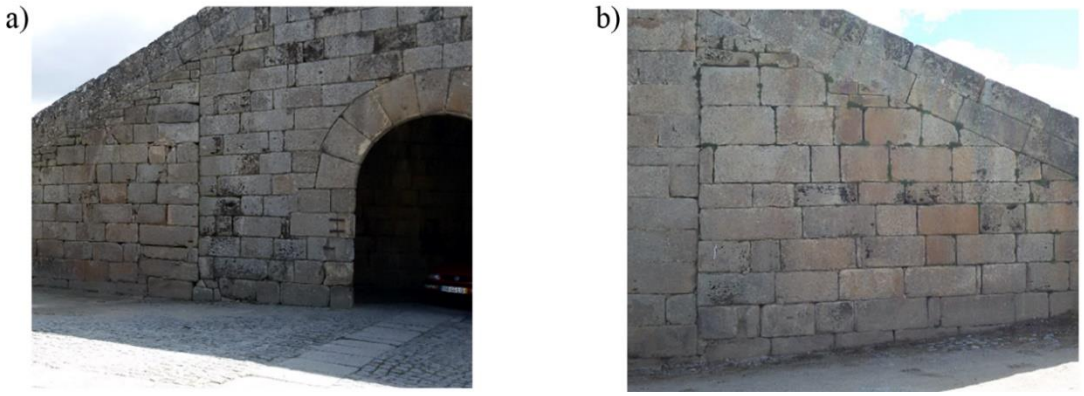

Figure 23: Construction defects observed on façade A: (a) on the left side; and (b) on the right side.

Concerning the roof, a large discrepancy with respect to the hypothetical original roof can be observed, with a maximum value of 0.21 m (Fig. 18). This disparity increases in the centre of the construction system (the part with less thickness) suggesting an accommodation of the infill and corroborating the significance of the reconstruction carried out during 1960 and 1986 (Fig. 9). The greatest deviations are due to the significant permanent deformations that occurred around the crack that is now apparently stabilized (Fig. 9b).

Finally, on the barrel vault, the high presence of salts and moistures (7.85% and 15.83% of the total surface) have promoted the disaggregation of the masonry blocks, especially in the intersection between the barrel vault and the façade B (Fig. 21), due to the atmospheric contamination and the infiltrations of salts and water derived from the infill placed on it. Part of these infiltrations, specifically 12.34% of them, are present on the most eroded parts of the barrel vault (Fig. 22b).

In general, the analysis of the deformations does not show any significant problem with the structure of the gate. Most of the deformations are construction defects promoted by the different restorations of the Master Gate. Additionally, it is necessary to highlight that both façades show large areas with black deposits and nitrophilic lichens affecting mainly the aesthetic of the façades. These damages, can be remove by compatible cleaning strategies. It is also important to fill the areas covered by lichens since these areas are more vulnerable to water infiltration and

chemical attacks. Concerning the state of conservation of the barrel vault, relevant damage indicators (presence of white crusts, black deposits and disaggregation) are promoting important material losses so this part of the gate requires urgent work such as roof waterproofing and joint filling (with a compatible mortar) to avoid structural problems and further material losses.

6 Conclusions

At present, damage mapping in historical constructions requires a large user interaction to first identify the damages presented on the monument and later to map them on 2D products such as sections, plants or elevations. To solve these limitations, the present paper shows a methodology based on the results captured by a TLS system (3D environment), that can combine radiometric and geometric procedures with the aim of detecting a wide diversity of pathological processes commonly presented on masonry construction.

On one hand, the radiometric analysis of the point clouds, by means of the TLS calibration as well as the Fuzzy-k-means method, proves to be a potential solution to the detection of certain types of pathological processes (such as biological colonization, salts or moisture), showing great correlation with those pathological processes observed during the visual inspection.

On the other hand, geometrical strategies such as the PCA analysis, the RANSAC approach or the CANUPO algorithm can work with geometrical features presented on the point cloud, allowing the extraction of planes or areas with strong material losses.

The combination of both approaches offers new possibilities in the diagnosis of the conservation state of our Cultural Heritage. By using this methodology, we demonstrated the ability not only to evaluate the damage in a 3D environment but also the high correlation between visual indicators of damages and results after analysing the multilayer point cloud.

Regarding the case study evaluated, the time invested to create the multilayer point cloud, in an Intel® Core i5-3750K @ 3.40 GHz with 32 Gb of RAM memory, was approximately 14.75 hours: (i) 5.5 hours to capture the structure (composed of 26 scan stations) and (ii) 9.25 hours to post-

process the data (6.0 hours of computer time and 3.25 hours of user time). The results obtained for this field campaign corroborate the advanced state of degradation of the Master Gate. This fact becomes more evident in the barrel vault, where there is a strong presence of salt crusts and areas with high levels of moisture.

Considering the complexity of the diagnosis of the construction as well as the advantages and limitations offered by the proposed method, future work will be focused on the following fields: (i) radiometry; (ii) geometry; (ii) sensor integration; and (iv) visualization and management.

Regarding the radiometric aspect, further work will be focused on the integration of additional sensors such as RGB or multispectral cameras, allowing a better separability between classes.

With respect to the geometrical features, further investigations will be focused on the design of additional filters for the CANUPO algorithm, using the sharpness concept or the density of the point cloud.

For sensor integration, data fusion of other non-destructive tests such as Ground Penetrating Radar, boroscopic cameras or Scanning Electron Microscopes will be assessed to evaluate possible internal defects present in the construction. The focus will be the creation of a methodology for an accurate and complete diagnosis of the state of conservation of historical masonry buildings, with the San Francisco Master Gate being one of the case studies. Finally, such a large amount of data will be introduced into a multitemporal Geographical Information System or Building Information Model to assist in the decision making.

Acknowledgments

This work was financed by FEDER funds through the Competitiveness Factors Operational Programme - COMPETE and by national funds through FCT – Foundation for Science and Technology within the scope of the project POCI-01-0145-FEDER-007633. This research has been also partially supported by CHT2 – Cultural Heritage through Time – funded by JPI CH Joint Call and supported by the Ministerio de Economia y Competitividad, Ref. PCIN-2015-071.

605

606 **References**

607

608 [1] D.T. Herbert, Heritage, tourism and society, Mansell Publishing, California, 1995.
609 ISBN: 978-0720121728
610
611 [2] V. Charter, International charter for the conservation and restoration of
612 monuments and sites, Second international congress of architects and technicians
613 of historic monuments, 1964. https://www.icomos.org/charters/venice_e.pdf
614
615 [3] L.F. Ramos, R. Aguilar, P.B. Lourenço, S. Moreira, Dynamic structural health
616 monitoring of Saint Torcato church, Mechanical Systems and Signal Processing
617 35 (1–2) (2013) 1-15. https://doi.org/10.1016/j.ymssp.2012.09.007
618
619 [4] B. Conde, L. Díaz-Vilariño, S. Lagüela, P. Arias, Structural analysis of Monforte
620 de Lemos masonry arch bridge considering the influence of the geometry of the
621 arches and fill material on the collapse load estimation, Construction and Building
622 Materials 120 (2016) 630-642.
623 https://doi.org/10.1016/j.conbuildmat.2016.05.107
624
625 [5] P. Rodríguez-Gonzálvez, J. Mancera-Taboada, D. González-Aguilera, Á. Muñoz-
626 Nieto, J. Armesto, A hybrid approach to create an archaeological visualization
627 system for a Palaeolithic cave, Archaeometry 54 (3) (2012) 565-580.
628 https://doi.org/10.1111/j.1475-4754.2011.00638.x
629
630 [6] M. Steiger, A.E. Charola, K. Sterflinger, Weathering and deterioration, In: S.
631 Siegesmund, R. Snethlage (Eds.), Stone in architecture, Springer, Berlin, 2011,
632 pp. 227-316. ISBN: 978-3-642-14475-2
633
634 [7] A. Drei, A. Fontana, Load carrying capacity of multiple-leaf masonry arches, In:
635 C.A. Brebbia (Ed.), Structural Studies, Repairs and Maintenance of Heritage
636 Architecture VIII, Wessex Institute of Technology, 2003, 864. ISBN: 978-1-
637 85312-968-1.
638
639 [8] V. Vergès-Belmin, T. Anson-Cartwright, E. Bourguignon, P. Bromblet, J. Cassar,
640 E. Charola, E. DeWitte, J. Delgado-Rodriguez, V. Fassina, B. Fitzner, Illustrated
641 glossary on stone deterioration patterns, Monuments and Sites XV (2008) 78.
642
643 [9] C.T. Grimm, Masonry cracks: a review of the literature, Masonry: Materials,
644 Design, Construction, and Maintenance, ASTM International, 1988.
645 https://doi.org/10.1520/STP27272S
646
647 [10] G. Cristinelli, The Krakow Charter. Principles for the conservation and restoration
648 of built heritage, Marsilio, Venice 2000.
649
650 [11] ICOMOS/ISCARSAH Commitee, Recommendations for the analysis,
651 conservation and structural restoration of architectural heritage, International
652 Scientific Committee for Analysis and Restoration of Structures and Architectural
653 Heritage (2003). See www.icomos.org

[12] J.A. Torres-Martínez, M. Seddaiu, P. Rodríguez-Gonzálvez, D. Hernández-López, D. González-Aguilera, A Multi-Data Source and Multi-Sensor Approach for the 3D Reconstruction and Web Visualization of a Complex Archaelogical Site: The Case Study of "Tolmo De Minateda", Remote Sensing 8 (7) (2016) 550. https://doi.org/10.3390/rs8070550

[13] B. Riveiro, P. Morer, P. Arias, I. De Arteaga, Terrestrial laser scanning and limit analysis of masonry arch bridges, Construction and Building Materials 25 (4) (2011) 1726-1735. https://doi.org/10.1016/j.conbuildmat.2010.11.094

[14] L.J. Sánchez-Aparicio, B. Riveiro, D. Gonzalez-Aguilera, L.F. Ramos, The combination of geomatic approaches and operational modal analysis to improve calibration of finite element models: A case of study in Saint Torcato Church (Guimarães, Portugal), Construction and Building Materials 70 (2014) 118-129. https://doi.org/10.1016/j.conbuildmat.2014.07.106

[15] J. Herráez, P. Navarro, J.L. Denia, M.T. Martín, J. Rodríguez, Modeling the thickness of vaults in the church of Santa Maria de Magdalena (Valencia, Spain) with laser scanning techniques, Journal of Cultural Heritage 15 (6) (2014) 679-686. https://doi.org/10.1016/j.culher.2013.11.015

[16] S. Del Pozo-Aguilera, J. Herrero-Pascual, B. Felipe-García, D. Hernández-López, P. Rodríguez-Gonzálvez, D. González-Aguilera, Multispectral Radiometric Analysis of Façades to Detect Pathologies from Active and Passive Remote Sensing, Remote Sensing 8 (1) (2016) 80. https://doi.org/10.3390/rs8010080

[17] E. Quagliarini, P. Clini, M. Ripanti, Fast, low cost and safe methodology for the assessment of the state of conservation of historical buildings from 3D laser scanning: The case study of Santa Maria in Portonovo (Italy), Journal of Cultural Heritage 24 (2016) 165-170. https://doi.org/10.1016/j.culher.2016.10.006

[18] P.J. Besl, N.D. McKay, Method for registration of 3-D shapes, IEEE Transactions on Pattern Analysis and Machine Intelligence 14(2) (1992) 239-256. https://doi.org/10.1109/34.121791

[25] T. Voegtle, S. Wakaluk, Effects on the measurements of the terrestrial laser scanner HDS 6000 (Leica) caused by different object materials, In: F. Bretar, M. Pierrot-Deseilligny, G. Vosselman (Eds), Laser scanning 2009, IASPRS, Paris, France, 1-2 September, 38 (2009) 68-74.

[19] R. Toldo, A. Beinat, F. Crosilla, Global registration of multiple point clouds embedding the Generalized Procrustes Analysis into an ICP framework, In: A. Bartoli, M. Magnor (Eds.), 5th International Symposium on 3D Data Processing, Visualization and Transmission (3DPVT'10), Paris, France, 17-20 May., (2010).

[20] L.J. Sánchez-Aparicio, S. Del Pozo, P. Rodríguez-Gonzálvez, J. Herrero-Pascual, A. Muñoz-Nieto, D. González-Aguilera, D. Hernández-López, Practical Use of Multispectral Techniques for the Detection of Pathologies in Constructions, In: B. Riveiro, M. Solla (Eds), Non-Destructive Techniques for the Evaluation of

Structures and Infrastructure, CRC Press, 2016, pp. 253-271. ISBN: 978-1-315-68515-1

[21] W. Wagner, A. Ullrich, V. Ducic, T. Melzer, N. Studnicka, Gaussian decomposition and calibration of a novel small-footprint full-waveform digitising airborne laser scanner, ISPRS Journal of Photogrammetry and Remote Sensing 60 (2) (2006) 100-112. https://doi.org/10.1016/j.isprsjprs.2005.12.001

[22] S. Kaasalainen, A. Jaakkola, M. Kaasalainen, A. Krooks, A. Kukko, Analysis of incidence angle and distance effects on terrestrial laser scanner intensity: Search for correction methods, Remote Sensing 3 (10) (2011) 2207-2221. https://doi.org/10.3390/rs3102207

[23] S. Soudarissanane, R. Lindenbergh, M. Menenti, P. Teunissen, Scanning geometry: Influencing factor on the quelity of terrestrial laser scanning, ISPRS Journal of Photogrammetry and Remote Sensing 66(4) (2011) 389-399. http://dx.doi.org/10.1016/j.isprsjprs.2011.01.005

[24] N. Pfeifer, B. Höfle, C. Briese, M. Rutzinger, A. Haring, Analysis of the backscattered energy in terrestrial laser scanning data, In: C. Jun, J. Jie, H.G. MAAS (Eds), XXIst ISPRS Congress, Beijing, China, 3-11 July, (2008) 1045-1052.

[25] T. Voegtle, S. Wakaluk, Effects on the measurements of the terrestrial laser scanner HDS 6000 (Leica) caused by different object materials, In: F. Bretar, M. Pierrot-Deseilligny, G. Vosselman (Eds), Laser scanning 2009, Paris, France, 1-2 September, 38 (2009) 68-74.

[26] S. Kaasalainen, A. Krooks, A. Kukko, H. Kaartinen, Radiometric calibration of terrestrial laser scanners with external reference targets, Remote Sensing 1 (3) (2009) 144-158. https://doi.org/10.3390/rs1030144

[27] J.C. Stover, Optical scattering: measurement and analysis,third ed., SPIE optical engineering press. Bellingham, 1995. ISBN: 9781628418408

[28] M. Dinguirard, P.N. Slater, Calibration of space-multispectral imaging sensors: A review, Remote Sensing of Environment 68 (3) (1999) 194-205. https://doi.org/*10.1016/S0034-4257(98)00111-4*

[29] B. Höfle, N. Pfeifer, Correction of laser scanning intensity data: Data and model-driven approaches, ISPRS Journal of Photogrammetry and Remote Sensing 62 (6) (2007) 415-433. https://doi.org/10.1016/j.isprsjprs.2007.05.008

[30] A.K. Jain, M.N. Murty, P.J. Flynn, Data clustering: a review, ACM computing surveys (CSUR) 31 (3) (1999) 264-323. https://doi.org/10.1145/331499.331504

[31] J.C. Bezdek, Fuzzy mathematics in pattern classification, PhD Thesis, Department of applied Math., Cornell University, New-York, 1973.

[32] D. Lague, N. Brodu, J. Leroux, Accurate 3D comparison of complex topography with terrestrial laser scanner: Application to the Rangitikei canyon (N-Z), ISPRS Journal of Photogrammetry and Remote Sensing 82 (2013) 10-26. https://doi.org/10.1016/j.isprsjprs.2013.04.009

[33] R. Schnabel, R. Wahl, R. Klein, Efficient RANSAC for point-cloud shape detection, Wiley Online Library, 26 (2007). 214-226. https://doi.org/10.1111/j.1467-8659.2007.01016.x

[34] N. Brodu, D. Lague, 3D terrestrial lidar data classification of complex natural scenes using a multi-scale dimensionality criterion: Applications in geomorphology, ISPRS Journal of Photogrammetry and Remote Sensing 68 (2012) 121-134. https://doi.org/10.1016/j.isprsjprs.2012.01.006

[35] J. Campos, Almeida, candidatura das fortificações abaluartadas da Raia Luso-Espanhola a património mundial–UNESCO, Câmara Municipal de Almeida,Almeida, 2009. ISBN: 978-989-95145-5-3

[36] F. Cobos-Guerra, Almeida-Ciudad Rodrigo: la fortificación de la raya central, Consorcio Transfronterizo de Ciudades Amuralladas, COAM, 2013. ISBN: 978-84-616-2665-6

[37] Núñez-García, Evaluation of structural intervention in the Quartel das Esquadras, Almeida (Portugal), Master´s Thesis, Department of Civil Engineering, University of Minho, Guimarães, 2015.

[38] G. Zhang, J.S. Strøm, M. Blanke, I. Braithwaite, Spectral signatures of surface materials in pig buildings, Biosystems engineering 94 (4) (2006) 495-504. https://doi.org/10.1016/j.biosystemseng.2006.05.002

[39] S.-J. Kim, A. Magnani, S. Boyd, Robust fisher discriminant analysis, In: Y. Weiss, P.B. Schölkopf, J.C. Platt (Eds.), Advances in Neural Information Processing Systems 18: Proceedings of the 2005 Conference (Neural Information Processing), MIT Press, 2006, pp. 659-666. ISBN:0262232537